

# Correlations between Dark Matter, Gas and Star Components of Halos in SPH Simulations

Pascal S. P. Steger<sup>1\*</sup>, Oliver J. Hahn<sup>2</sup>, C. Marcella Carollo<sup>1</sup>, Cristiano Porciani<sup>3</sup> and Giuseppe Tormen<sup>4</sup>

<sup>1</sup>*Department of Physics, ETH Zürich, CH-8093 Zürich, Switzerland*

<sup>2</sup>*KIPAC, Stanford University, 2575 Sand Hill Road, Menlo Park, CA 94025, USA*

<sup>3</sup>*Argelander-Institut für Astronomie, D-53121 Bonn, Germany*

<sup>4</sup>*Dipartimento di Astronomia, Università di Padova, Vicolo dell'Osservatorio 2, I-35122 Padova, Italy*

30 May 2010

## ABSTRACT

We quantify disalignment of angular momentum between gas, stars and dark matter components of halos in cosmological SPH-simulations in  $\Lambda$ CDM. Furthermore, we investigate correlations between angular momentum, inertia axes and the eigenvectors of the tidal field. These correlations will help to constrain contamination of weak lensing signals arising due to intrinsic alignment. The spin-parameter distributions with distinction between the three particle types and velocity dispersions allow us to estimate the influence of ordered rotation on these correlations.

We find: (1) a median angular momentum disalignment of  $76^\circ$  between the gas and the dark matter component and of  $59^\circ$  between stars and dark matter; (2) a correlation between the biggest eigenvector  $\mathbf{t}_1$  of the tidal field and total angular momentum that is similar, but less distinct than between  $\mathbf{t}_1$  and the main inertia axis; (3) the halo spin parameter of gas to be roughly an order of magnitude higher than the one of dark matter and stars.

**Key words:** cosmology: theory, large-scale structure of Universe – methods: numerical

## 1 INTRODUCTION

To describe the universe and its temporal evolution, to find the dark matter distribution and thereby to follow the galaxy formation history is the long-term goal of extragalactic astronomy. By starting from visible parts of galaxies, gas and stars, one has to infer all properties used in the overall description as e.g. mass, shape parameters and angular momentum. Using simulations one starts with a known distribution of dark matter, gas and stars and infers properties from them that can be used as predictions for observations. The available resources restrict the achievable resolution: If one wants to sample the matter distribution with high resolution, only relatively small scales are sampled; on the other hand there is only coarse resolution when working on the largest scales. Resimulations do circumvent this restriction partly: After a low resolution run on large scales an interesting region is selected and traced backwards to the initial conditions, which are resampled to higher resolution. The surroundings are kept at low resolution, thus providing the same large scale influence, but at lower computational cost. Figure 1 shows a snapshot of a resimulated cluster at  $z = 0$ , rendered with SPLOTCH<sup>1</sup>. Colors encode the internal energy of the gas particles, star density gives intensity.



**Figure 1.** Visualization by ray-tracing of one of the resimulated clusters. The visible box size spans a range of  $50 h^{-1} \text{Mpc}$ .

\* E-mail: psteger@phys.ethz.ch

<sup>1</sup> <http://dipastro.pd.astro.it/cosmo/Splootch>

One of the observable properties of galaxies that first spring into mind is its shape. In order to connect the measured shape of the baryons with the shape of the more influential dark matter part, we investigate the alignment of halo shape parameters with each other.

The temporal evolution of the shape is given, as pointed out by Valluri et al. (2010), by adaptations of individual particle orbits to the changing potential. The potential is changed by encounters with neighboring halos or by interaction with the large scale structure. All changes in particle orbits affect the angular momentum, which in turn can be observed from the rotation of the baryonic matter in the center of the halo. In this article we investigate alignments of shape parameters of components of the halo with each other as well as with angular momentum and the large scale structure.

It has been established by observations and reproduced in simulations that there are a number of significant alignments, indeed: In gravitational potentials of clusters, gas traces the shape of the dark matter halo pretty well outside the core (Lau et al. (2010)). Further away, it is found that the major axes of subhalos align with the direction to the center of mass of the respective host halo (Yang et al. (2006), Faltenbacher et al. (2007), Faltenbacher et al. (2008)), indicating a contribution from small scale gravitational influence. On bigger scales, Wang et al. (2008) found alignments between the major axes of host galaxies in neighboring groups as well as impact on the alignments of satellites. Aragón-Calvo et al. (2007) indicate that the minor axes tend to lie perpendicular to the host structure. On the very biggest scales, Basilakos et al. (2006) find an alignment between cluster and supercluster major axes, while Cuesta et al. (2008) report that halos on the shells of voids preferentially align their angular momentum and shape perpendicular to the direction joining halo and void center.

In order to understand the evolution of galaxies one has to account for the buildup of dynamical properties as e.g. angular momentum. Peebles (1969) showed that the angular momentum observed nowadays agrees with galaxy formation through gravitational instability. Starting from Gaussian initial conditions at early time, tidal torques of large scale structures induce torquing on smaller structures and seed the first buildup of angular momentum, see e.g. Barnes & Efstathiou (1987) for simulations with different initial conditions.

The contributions to angular momentum by dark matter, gas and stars differ considerably:

Angular momentum of dark matter is mainly conserved; simulations performed by e.g. Sharma & Steinmetz (2005) indicate that roughly half of the dark matter is rotating in the same sense as baryonic matter, while the other half is counterrotating.

The fact that a net angular momentum is observed in galaxies suggests that there exists a process to enhance angular momentum for stars and gas. The configuration with smallest energy for a self-gravitating system with given angular momentum is a disk, which is observed in late type galaxies, after a big amount of internal energy of the gas is radiated away. Stars in elliptical galaxies have left the disks due to orbit instabilities encountering external gravitational influences. Violent relaxation then leads to the observed number density distribution; the angular momentum in the central parts of halos is increased by transferring some small fraction of the halo mass outwards.

With numeric simulations, one tries to quantize the history of angular momentum buildup and transformation between the different components. Sharma & Steinmetz (2005) investigate the angular momentum disalignment of the gas and dark matter components of halos in a nonradiative  $N$ -body/SPH simulation and find a mis-

alignment of typically  $20^\circ$ . Croft et al. (2008) included disalignments between star and dark matter components in the analysis at  $z = 1$  and found median values of  $43.5^\circ$  for stars and  $69.6^\circ$  for gas. With a simulation up to  $z = 0$ , we are able to compare with the previous results and search for dependences on halo mass. Halos in the near vicinity of larger halos experience gravitational forces that influence their orientation, e.g. by precession. As subhalos fly by the core of their host, they reorient themselves with respect to its center, given that the typical rotation timescale is smaller than the time to cross the big structure. See Pereira et al. (2008) for a reference. This work quantifies alignment between particle types as function of radial separation, measured in terms of the virial radius of the host.

The distribution of the disalignment angle as found in numerical simulations e.g. by van den Bosch et al. (2002) leave an imprint on the measured intrinsic alignments that attribute to weak lensing signal. This is used in future high-precision studies of dark energy, see e.g. Catelan et al. (2001) for the contamination from large-scale alignments with ranges of 1 to 100 Mpc and Hirata et al. (2004) for the shear-ellipticity alignment. Estimates for intrinsic alignments as function of redshift and environment therefore help to deduce the large scale structure of dark matter from observations. The environment in which a halo resides is part of the cosmic web: vast regions called voids with low density, embedded in sheets of higher density at their borders, which meet in filaments which in turn are connected by dense clusters (cf. Tegmark et al. (2004) for two galaxy surveys, Shandarin & Zeldovich (1989), Bond & Myers (1996)). This cosmic web follows from Gaussian perturbations in the early stage of the universe through collapse along the main axes of the strain tensor, cf. Zel'Dovich (1970) for a first order approximation.

Brunino et al. (2007) and Cuesta et al. (2008) report on a mean alignment between the angular momentum and the radial direction to the nearest void in numerical studies. Hahn et al. (2010) quantify the alignments of halos inside a filamentary structure at redshifts  $z = 1, 0.5, 0$ . They find that massive galaxy disks have spins aligned with the filament. To measure this kind of alignment, one has to consider the structure of the tidal field. Its imprint on the orientation of the galaxies today is best described by tidal torque theory, which gives expressions for the two-point correlation function of the tidal field (Porciani et al. (2002a), Porciani et al. (2002b) and references). Schaefer (2008) gives an overview of the connections between tidal torquing and angular momentum acquisition as well as the resulting angular momentum distribution. With our work we are able to probe alignments of the baryonic parts of the galaxies with the tidal field on arbitrary scales, concentrating on  $1 h^{-1}$  Mpc.

The rest of the paper is laid out as follows: Chapter 2 gives an overview over the specifications of the simulations under consideration; definitions and methods are laid down in chapter 3. In chapter 4 we present our results for the disalignment between angular momentum, main inertia axis and tidal field eigenvectors. It follows a summary in chapter 5; we conclude the work with propositions for further investigations. The appendix contains comparisons of the two calculation methods given by our definitions and AHF, while checks for numerical and statistical artefacts are described directly with the results.

## 2 THE DATA

### 2.1 Specifics of the Simulations

We use high-resolution cosmological hydrodynamic simulations of three individual galaxy clusters – see figure 1 for a visualiza-

Simulation	$M_{\text{vir}}/h^{-1}\text{M}_{\odot}$	$R_{\text{vir}}/h^{-1}\text{Mpc}$	$N_{\text{sub}}$	$N_{\text{field}}$
c1	$2.8900 \times 10^{14}$	1.3466	502	218
c2	$1.6021 \times 10^{14}$	1.1062	279	200
c3	$2.4922 \times 10^{14}$	1.2817	399	163

**Table 1.** Properties of the resimulated clusters.  $M_{\text{vir}}$  and  $R_{\text{vir}}$  are the virial mass and radius of the clusters. The number of subhalos above  $M = 5 \cdot 10^9 h^{-1}\text{M}_{\odot}$  within the cluster virial radius is given by  $N_{\text{sub}}$ , while  $N_{\text{field}}$  is the number of isolated halos above  $M = 5 \cdot 10^9 h^{-1}\text{M}_{\odot}$  within 3 virial radii from the cluster center.

tion of a low-resolution run of cluster 3 – embedded in a cosmological box of  $192 h^{-1}\text{Mpc}$ . The cosmological model assumes a flat  $\Lambda\text{CDM}$  cosmology with matter density parameter  $\Omega_m = 0.3$ , baryon fraction  $\Omega_b = 0.04$ , Hubble constant  $H_0 = hH_{100} = 70 \text{ km s}^{-1} \text{ Mpc}^{-1}$  and a power spectrum normalization of  $\sigma_8 = 0.8$ . The simulations were performed using the tree-SPH+ $N$ -body code GADGET-2 (Springel 2005) and include subgrid models for cooling, star formation and stellar feedback identical to the simulations described by Borgani et al. (2004). AGN feedback is not included, so the density inside the halo centers is enhanced due to overcooling. As shown by Sales et al. (2010) recently, this effect increases the mass of a halo by a factor  $\pm 10$ . The angular momentum of the galaxy being roughly half the one of the surrounding halo is however largely independent of halo mass and feedback scheme. We conclude that angular momentum and principal axes are not considerably changed.

The three galaxy clusters were resimulated at 45 times higher resolution giving a mass resolution of  $1.03 \times 10^7 h^{-1}\text{M}_{\odot}$  for the dark matter component, while gas and stars were both sampled with particles of mass  $7.7 \times 10^6 h^{-1}\text{M}_{\odot}$ . Dark matter particles in the outskirts of the simulation box have varying masses above  $5.33 \times 10^9 h^{-1}\text{M}_{\odot}$ . Spatial smoothing is performed over a Plummer equivalent’s width of  $7.5 h^{-1}\text{kpc}$ .

All simulations started at  $z = 100$  and evolved until  $z = 0$  where we perform the analysis. The properties of the three resimulated clusters at  $z = 0$  are summarized in table 1.

## 2.2 Halo and Subhalo Samples

Halos and subhalos in the high-resolution region were identified with the AMIGA halo finder (Knollmann & Knebe (2009) and Gill et al. (2004)) that identifies a hierarchy of gravitationally bound density peaks:

Starting from local density minima or leaves of an adaptive mesh refinement hierarchy all particles in a sphere around this point are included, out to a radius where the density falls below  $\Delta_{\text{vir}}\bar{\rho}$ , as defined by Bryan & Norman (1998). Additionally, particles residing in a lower density environment – or equivalently in a higher level in the AMR tree – are assigned to the nearest halo of the same level. The halo edge is determined as the contour at which the density starts to rise again. Particles that happen to lie in the realm of a halo but are not gravitationally bound are removed iteratively; the halo properties are calculated from the remaining sample, by integrating over logarithmically spaced shells centered on the center of mass.

In order to treat near encounters correctly, where we center on the most bound particle instead on the center of mass, we implemented an additional procedure to remove still unbound particles iteratively, as proposed by Porciani et al. (2002a): The most

unbound particle is excluded, potential and kinetic energy get recomputed, then the next most unbound particle is searched for. Excluded particles are allowed to reenter the halo at a later step if they get bound again. A mean fraction of 3% of the particles is excluded in addition to the unbinding procedure from AMIGA in the low resolution run; the main contribution coming from low mass halos, as the gravitational potential generated from particles outside the virial radius is completely neglected by such an approach. We find that contamination from a few virially unbound particles – especially gas particles with too high internal energy – is less important than the error induced from lower particle numbers for the smaller halos and the gas and star components with low resolution. Therefore, the procedure is not invoked for computations including gas and star particles.

We computed the complete subhalo tree using MERGERTREE to find particles shared by several halos in the same simulation snapshot and searching the respective host halo as the one which owns the highest fraction of particles residing in a given halo.

A total of 11% of the halos are assigned to a host halo; all other halos are considered single halos. Searching for correlations between subhalos and their host we analyze the properties of these single halos with respect to the halo residing in the cluster center of each simulation and afterwards stack the resulting values for analysis.

For each halo we determine the shape and angular momentum of gas, stars and dark matter as described in the next chapter. If not specified otherwise, the figures were created using particles of all types together. For our analysis, we stack the halos of all three clusters and restrict ourselves to halos that have more than 200 dark matter, more than 10 gas and star particles inside. Moreover, we exclude all halos that contain low resolution dark matter particles with a mass bigger than 1% of the halo mass. This exclusion mainly applies for small halos in the outer regime of the simulation box where low resolution particles – with an overall occurrence of only 0.07% – can dominate determination of the halo properties.

## 3 DEFINITIONS

### 3.1 Shapes

The shape of a halo with  $N$  particles is determined by its weighted moment of inertia tensor (see e.g. Hahn et al. (2007), Porciani et al. (2002a)),

$$I_{jk} \equiv \sum_{i=1}^N m_i (r_i^2 \delta_{jk} - (x_i)_j (x_i)_k) \quad (1)$$

with the distance  $r_i \equiv ((x_i)_1, (x_i)_2, (x_i)_3)$  of a particle at position  $x_i$  from the center of mass. Written in an eigensystem with eigenvectors  $\mathbf{e}_1, \mathbf{e}_2, \mathbf{e}_3$ , it reads as

$$\tilde{I} = \frac{M}{5} \cdot \text{diag}(\ell_1^2 + \ell_3^2, \ell_1^2 + \ell_3^2, \ell_2^2 + \ell_3^2) \quad (2)$$

with the lengths of the principal axes  $\ell_1 \geq \ell_2 \geq \ell_3$ . All computations of correlation functions use the corresponding eigenvectors normalized to 1, while the degeneracy stemming from multiplication of -1 is removed using absolute values.

### 3.2 Angular Momentum

The classical definition of

$$\mathbf{J} \equiv \sum_{i=1}^N \mathbf{r}_i \times m_i \mathbf{v}_i \quad (3)$$

is used to calculate the angular momentum in the center of mass frame. The sum in (3) goes over all bound particles of the halo, out to the virial radius. We note that particles with a mass fraction of 8.5% are excluded by a spherical overdensity criterion in comparison with all particles assigned to the respective halo.

AMIGA uses a slightly different method with averaging over concentric shells around the center of mass with logarithmic spacing, resulting in a slightly higher value for the angular momentum. We use the classical sum, as the radius from the center of mass is computed for each particle separately.

An additional quality improvement that we shall include in a future work is inclusion of bound particles outside the sphere of  $\rho > \Delta(z)\rho_{\text{mean}}$ .

### 3.3 Halo Spin Parameter

Following Bullock et al. (2001), we define the spin parameter

$$\lambda' \equiv \frac{|\mathbf{J}|}{\sqrt{2}MRV} \quad (4)$$

with the angular momentum  $\mathbf{J}$  inside a sphere of radius  $R$ , mass  $M$  and circular velocity  $V$ . We have  $V^2 = GM/R$  if the halo is in dynamical equilibrium and therefore

$$\lambda' = \frac{|\mathbf{J}|}{\sqrt{2}GRM^{3/2}}, \quad (5)$$

where  $J$  and  $M$  are calculated from particles inside a sphere around the most bound particle, with radius  $R_{\text{vir}}$ . Inside this sphere  $\rho < \Delta(0)\rho_{\text{crit},0}$ , with  $\Delta(z)$  given by (Bryan & Norman 1998)

$$\Delta(z) = 18\pi^2 + 82f(z) - 39f^2(z) \quad (6)$$

$$f(z) = -\frac{\Omega_\Lambda}{\Omega_m(1+z)^3 + \Omega_\Lambda} \quad (7)$$

Bullock et al. (2001) established that  $\lambda'_{\text{DM}}$  is best described by a log-normal distribution,

$$p(\lambda)d\lambda = \frac{1}{\sqrt{2\pi}\sigma_\lambda} \exp\left[-\frac{\ln^2(\lambda/\bar{\lambda})}{2\sigma_\lambda^2}\right] \frac{d\lambda}{\lambda}, \quad (8)$$

which is a simple parabola  $y = ax^2 + bx + c$  in a logarithmic plot. This distribution is found to be robust under varying measures for the radius of the sphere. We use the same definition for gas and star components.

### 3.4 Rotation support

Rotationally supported spherical systems can be distinguished from systems with random motion by the ratio  $\Sigma/V_{\text{rot}}$ , with the velocity dispersion

$$\Sigma = \sqrt{\sum_{r_i < R_{\text{vir}}} \langle v_i^2 \rangle - \langle v_i \rangle^2} \quad (9)$$

and the rotation velocity  $V_{\text{rot}}$  of the particles in dynamical equilibrium at the virial radius from the halo center. The lower the velocity dispersion with respect to the virial velocity, the more particles move in the same manner and hence the bigger is the rotation support.

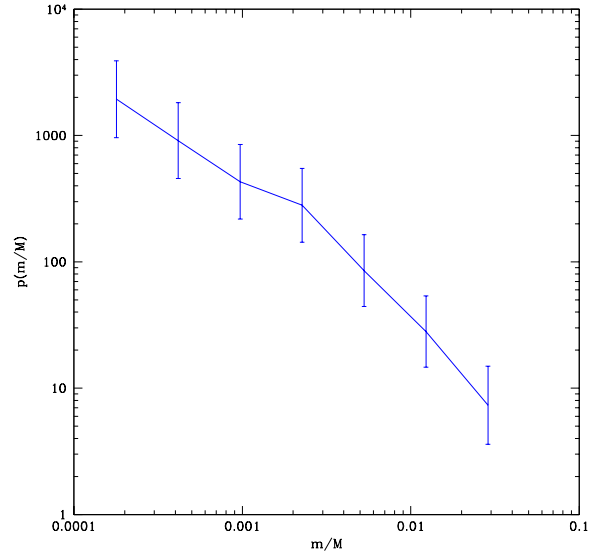


**Figure 2.** Differential subhalo mass function incorporating all particle types,  $\log_{10} p(m/M) \propto dn(m/M)/d \log_{10} m/M$ , where  $m$  is the mass of the subhalo,  $M$  of its host.

### 3.5 Tidal Field

We compute the local eigenstructure of the smoothed tidal field tensor at the position of each halo in order to probe the alignment with the large-scale structure (cf. Hahn et al. 2007). First, we solve Poisson's equation by Fast Fourier Transform on a grid of  $512^3$  cells for the smoothed overdensity field  $\delta = \rho/\bar{\rho} - 1$  by the double convolution  $\phi_R = \delta \star W_R \star G$ , where  $G$  is the Green's function of the symmetric 3-point finite difference operator and  $W_R$  is the window function of scale  $R$  used to smooth the density field, top hat or Gaussian. The tidal tensor

$$T_{ij}(\mathbf{x}) \equiv \left[ \partial_i \partial_j - \frac{1}{3} \delta_{ij} \nabla^2 \right] \phi(\mathbf{x}) \quad (10)$$

is then evaluated at the positions of the halo centers by finite differencing. We finally compute eigenvalues  $\tau_1 \leq \tau_2 \leq \tau_3$  and corresponding eigenvectors  $\mathbf{t}_1, \mathbf{t}_2, \mathbf{t}_3$  for each halo. Halos with three positive eigenvalues correspond to clusters, filaments have one negative eigenvalue, sheets two and voids with unstable orbits have no positive eigenvalues.

### 3.6 Angle

We measure the angle between two vectors  $\mathbf{p}, \mathbf{q}$  by its cosine,

$$\phi(\mathbf{p}, \mathbf{q}) \equiv \frac{\mathbf{p} \cdot \mathbf{q}}{|\mathbf{p}| \cdot |\mathbf{q}|}. \quad (11)$$

Eigenvectors of the inertia tensor after normalization are degenerate up to a factor  $\pm 1$ . When correlating them with other vectors, we therefore will use the absolute value of  $\phi$ .

## 4 RESULTS

### 4.1 Subhalo Mass Function

The differential subhalo mass function as shown in figure 2 is in good agreement with a power law of slope  $-1$ , cf. De Lucia et al.

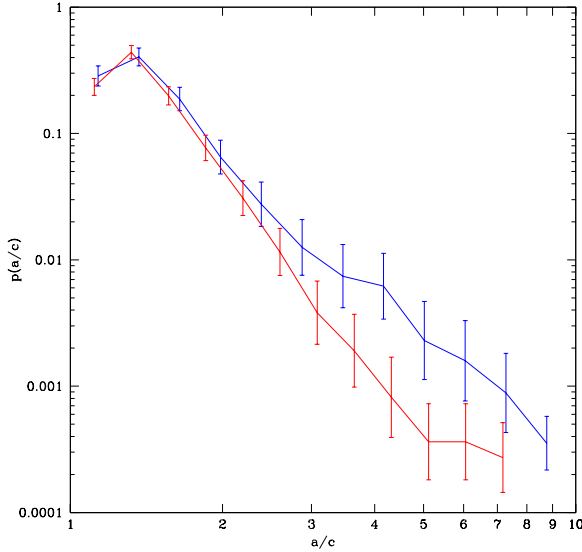


**Figure 3.** Inverse sphericity  $\ell_1/\ell_3$ . Blue points represent values from AHF, red points correspond to values computed with our framework. See text for further explanations.

(2004). Note that all subhalos with mass  $m$  of a host halo of mass  $M$  such that  $\log_{10}(m/M) < -4$  are excluded: below this threshold the discreteness of the halo constituents and their composition of particles with different masses imply that too little subhalos of a given mass are counted.

#### 4.2 Shape: Sphericity

In figure 3 we have plotted the distribution of the inverse sphericity  $1/S = \ell_1/\ell_3$ . Strictly spherical systems with  $a \approx c$  are slightly depressed, over all bins starting from the second we are consistent with a power law of slope  $-5.4 \pm 0.3$ . We have plotted the results of our framework as well as the results from AMIGA as an example for the correspondances and the differences between both calculation methods. These are discussed further in the appendix. For highly nonspherical systems the difference between center of mass (as used by AMIGA) and the position of the most bound particle (as used by our framework) begin to differ, mainly for halos with lower resolution.

#### 4.3 Shape: Radial Dependence

Figure 4 presents the radial alignment of the main inertia axis of the dark matter component with the radial vector as function of distance, as investigated previously by Pereira et al. (2008) in dark matter only simulations.

Two mass bins with all halos above and below  $M = 10^{11} h^{-1} M_\odot$  are shown. The splitting point in mass is chosen such that all halos with smaller mass do not host a hot pressurized atmosphere that exerts ram pressure on the central galaxy (Hahn et al. (2010) and references).

We recover the expected behavior for dark matter in the low mass range ( $m < 10^{11} M_\odot$ ), and find an even stronger correlation with a maximum around  $r \gtrsim R_{\text{vir}}$  for the high mass range; at radii

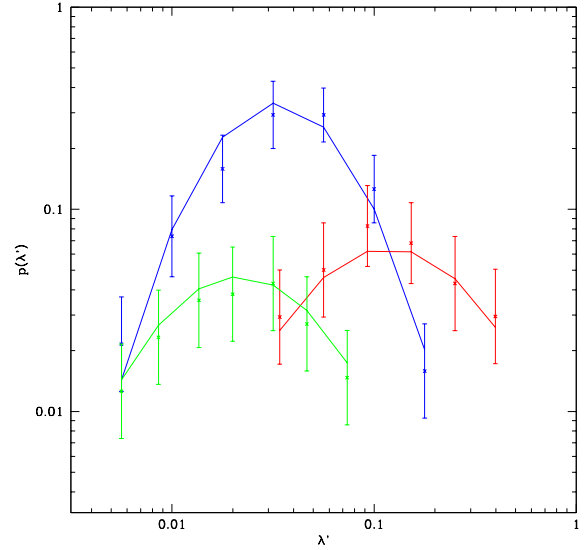


**Figure 5.** Halo spin parameter distribution for host halos, with fitted parabolas. Dark matter produces the blue line, stars the green one, gas is shown in red. See table 4.4 for fitting parameters.

higher than  $2R_{\text{vir}}$  the distribution is not significantly differing from an isotropic distribution with  $\phi(\mathbf{r}, \mathbf{e}_1) = 0.5$ .

Gas in high mass halos follows the trend for alignment at distances smaller than the virial radius of the host, but fails to maintain this alignment outside the virial radius. The upturn at  $r/r_{\text{vir}} > 2$  is produced possibly by massive halos in the outskirts of the cluster, as the exclusion criterion for gas restricts the analysis to massive halos, while most of the halos with large  $r/r_{\text{vir}}$  are analyzed with respect to the cluster center. Indeed, the low mass sample shows no significant upturn in these regimes.

Stars show a distinguished peak at low mass, which decays with distance out to  $r/r_{\text{vir}} = 2$ . Surprisingly, it shows stronger alignment than dark matter at small distances; in the high mass regime, this trend is not observed. We suggest that the creation of star particles at relatively late times, when there exists a pronounced environment, lets them feel the influence on small scales more strongly than the surrounding dark matter halo; this effect seems to be stronger for low mass halos, as indicated by the fact that dark matter in the high mass sample follows this trend out to an even larger radius.

#### 4.4 Kinematics: Spin parameter

Figure 5 shows the  $\lambda'$  distribution for dark matter, gas and stars. Additional tails at high values of  $\lambda'$  were removed by centering on the most bound particle instead of on the center of mass. With this procedure the ordered motion due to a close encounter with another halo is suppressed, cf. Hahn et al. (2007).  $\lambda'$  shows a log-normal distribution for dark matter, gas and stars; the maxima lie at  $-1.5$  for dark matter and stars and at  $-1$  for gas, respectively. Dark matter only simulations as e.g. by Bullock et al. (2001) show a peak at  $\lambda' = 0.035$ ,  $\log_{10} \lambda' \approx -1.46$ , indicating that inclusion of baryons does not change the dm angular momentum by huge amounts. If a parabola  $y = ax^2 + bx + c$  is fitted through these points, one gets the parameters listed in table 4.4.

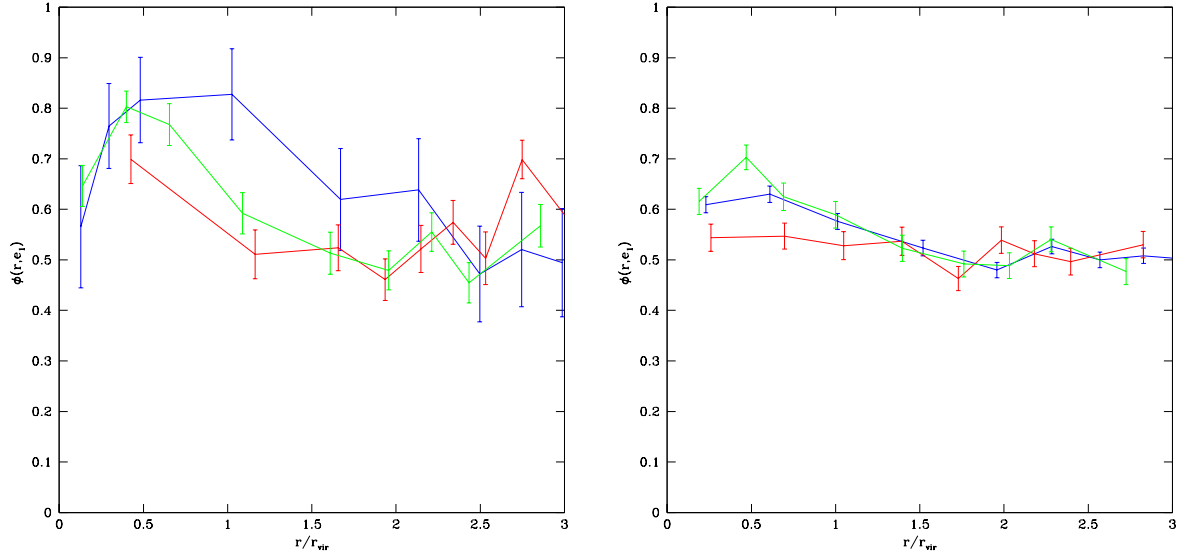


**Figure 4.** Distance dependence for the alignment between the main inertia axis  $\mathbf{e}_1$  and the radial vector  $\mathbf{r}$  to the cluster center. Panels on the left side include all halos with mass  $m \geq 10^{11} M_\odot$ , panels on the right side take all halos into account with  $m < 10^{11} M_\odot$ . Dark matter, gas and stellar components are shown in blue, red and green color.

Halo Type	$a$	$b$	$c$
Dark Matter	$-2.3 \pm 0.7$	$-6.7 \pm 2.0$	$-5.5 \pm 1.4$
Gas	$-1.4 \pm 0.6$	$-2.6 \pm 1.1$	$-2.4 \pm 0.5$
Stars	$-1.5 \pm 0.5$	$-5.0 \pm 1.8$	$-5.5 \pm 1.5$

**Table 2.** Fit parameters for  $\lambda'$ -distribution  $\log_{10} p(\lambda') = a(\log_{10} \lambda')^2 + b(\log_{10} \lambda') + c$  with errors for 95% level certainty.

The gas particles show a higher maximum for  $\lambda'$  and therefore more ordered motion compared to random motion. This fact is expected as the kinetic energy between gas particles is transformed into heat which in turn escapes through radiation. The distribution for stars peaks at roughly the same place as the one for dark matter, indicating that they rearranged in the potential dominated by dark matter after they were created out of gas particles.

#### 4.5 Kinematics: Rotation Support

For different particle types we find different rotation support: from figure 6 one clearly sees that dark matter has little rotation support, gas by contrast peaks at lower  $\Sigma/V$  and therefore shows more ordered rotation. Stars lie in between these two extremes. The smallest values of dark matter halo components start below  $\Sigma/V = 1$ , but they are so rare that the first bin shows highest abundance at  $\Sigma/V = 0.9$ . Gas shows a flatter distribution, in fact, they are the dominant contribution for high  $\Sigma/V$ . This is explained by the small gas mass, which enters with  $V = \sqrt{GM/R}$ , where  $R$  is the virial radius of the whole halo.

#### 4.6 Kinematics: Angular Momentum

We find that the angular momenta of the dark matter halos and the star constituents do well correlate with each other, with a median

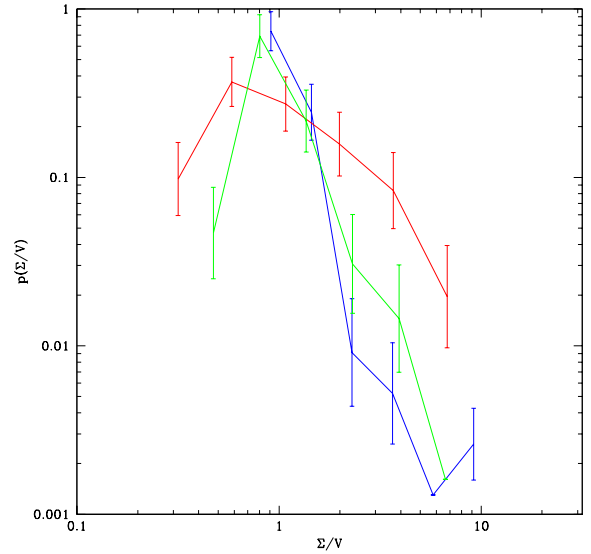


**Figure 6.**  $\Sigma/V$  split up into dark matter (blue), gas (red) and stars (green). Error bars show Poissonian errors.

angle of  $59^\circ$ . Gas angular momentum is inclined by a median  $76^\circ$  with respect to dark matter. To compare with observations, we need to add up stars and gas as baryonic, visible parts. The angular momentum disalignment of  $\phi(\mathbf{j}_{\text{dm}}, \mathbf{j}_{\text{bary}})$  is shown in figure 7. There are only little negative values for  $\phi$ , which contribute all less than the value for an isotropic distribution of 7.7%, indicating that counterrotation is suppressed.

We searched for a dependence of this alignment on radial distance and mass: Figure 8 shows the alignment as function of  $r/r_{\text{vir}}$ , where  $r$  is the distance from the host halo and  $r_{\text{vir}}$  is the virial ra-

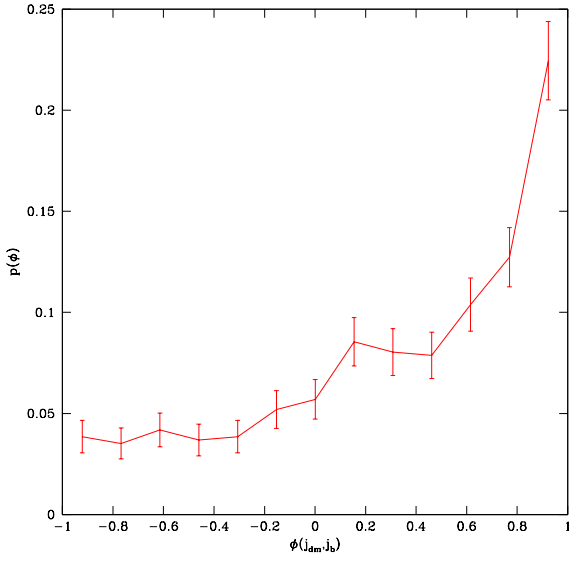


**Figure 7.** Distribution of angle  $\phi$  between the angular momentum axis of dark matter and baryonic halo components.

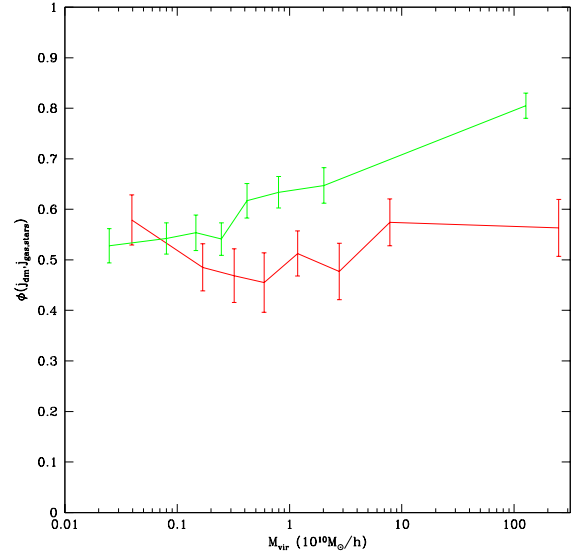


**Figure 9.** Correlation between  $\mathbf{j}_{\text{dm}}$  and  $\mathbf{j}_{\text{gas}}$  in red,  $\mathbf{j}_{\text{star}}$  in green as function of halo mass.

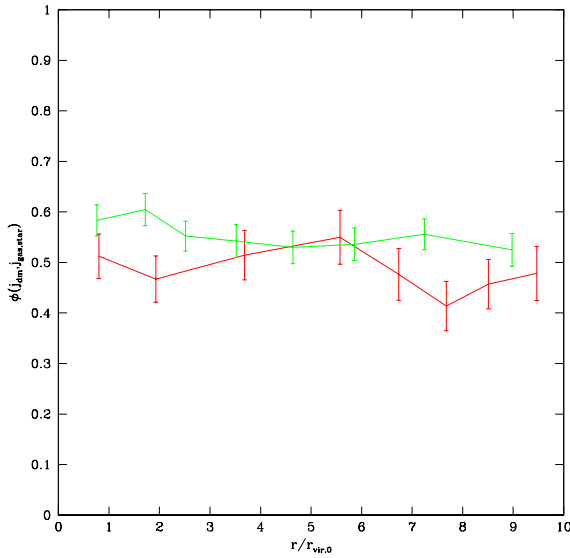


**Figure 8.** Correlation between  $\mathbf{j}_{\text{dm}}$  and  $\mathbf{j}_{\text{gas}}$  in red,  $\mathbf{j}_{\text{star}}$  in green as function of distance to cluster center.

dius of the host. The wide range plotted for  $r/r_{\text{vir}}$  allows to include halos in the outskirts of the main clusters, which are not assigned a host halo. One assumes, though, that the influence on alignment drops rapidly with distance and is practically negligible for  $r/r_{\text{vir}} > 3$ .

There is an alignment between  $\mathbf{j}_{\text{dm}}$  and  $\mathbf{j}_{\text{star}}$  near the host halo, where  $r/r_{\text{vir}} \approx 1$ . This alignment extends out to  $r/r_{\text{vir}} = 2.5$  for dark matter and stars; gas does not seem to be aligned as much. It does not show any alignment with significance over  $2\sigma$ , independent on radius.

As shown in figure 9 – where we adjusted the mass bin size to

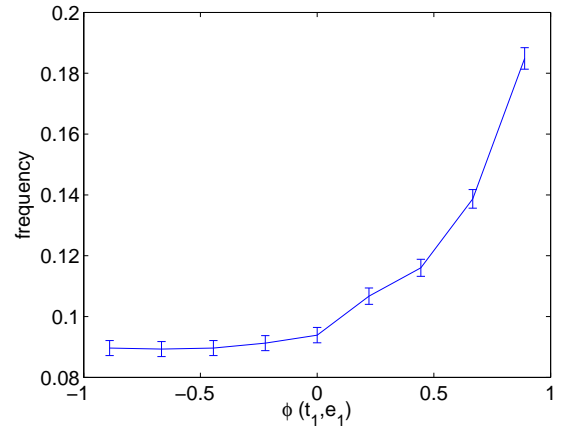


**Figure 10.** Correlation between  $\mathbf{t}_1$ , tidal field eigenvector corresponding to  $\tau_1$ , and main inertia axis  $\mathbf{e}_1$ . The smoothing scale for the tidal field is  $1 h^{-1} \text{Mpc}$ .

include the same number of halos – we find a trend for stronger alignment between angular momentum of stars and dark matter for increasing mass; the same conclusion cannot be drawn for gas, which is not significantly different from an isotropic distribution. A small enhancement in the very low and high mass regime is observed, though, indicating that halos with low gas fraction follow the overall behavior a little more likely than halos with a relatively high gas fraction.

#### 4.7 Tidal Field

We were able to reproduce the expected correlation between different components of the tidal field eigenvectors and the inertia axes, cf. Porciani et al. (2002b). One of the strongest correlations is shown in figure 10, where the tidal field smoothed over  $1 h^{-1} \text{Mpc}$



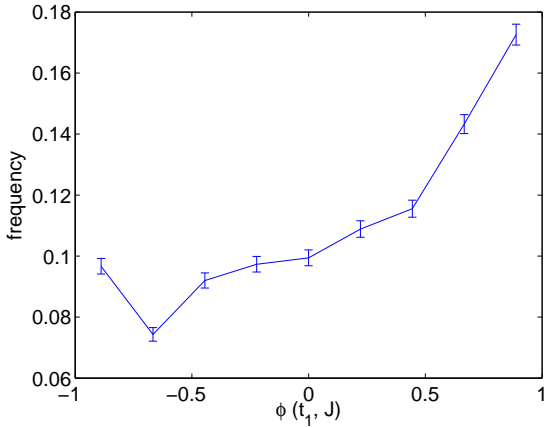


**Figure 11.** Correlation between  $t_1$  and angular momentum  $\mathbf{J}$  for a smoothing scale of  $1 h^{-1} \text{Mpc}$

and evaluated at the position of each halo is compared with the main inertia axis.

We found a similar correlation between tidal field and angular momentum, illustrated in figure 11. This is no surprise, given that  $\mathbf{J}$  points roughly in the direction of a characteristic inertial eigenvector – which in turn is supported by e.g. Croft et al. (2008) with a detected median angle of  $48.3^\circ$ .

## 5 SUMMARY AND DISCUSSION

We began by calculating the differential subhalo mass function and found it consistent with a power law of slope  $-1$ .

Next we considered the shape of the galaxies by both the sphericity and the radial dependence of alignment between the halo constituents inertia axes and radial vector to the host. Sphericity follows a powerlaw. On small radii the distribution of the angle between inertia axes and radial vector is not consistent with an isotropic one, with strong alignment for massive halos in comparison with smaller ones. Stars are aligned even stronger than the dark matter in low mass halos, due to their relatively recent rearranging to the enhanced large scale structure.

Kinematical properties were studied with the spin parameter distribution, rotation support and alignment of angular momenta. The spin parameter was found to have a log-normal distribution for all components, with roughly the same peak position for dark matter and stars and a peak for gas that lies an order of magnitude higher, indicating more ordered rotation. This is confirmed by direct measurement of ordered rotation for the three components, where dark matter shows practically no ordered rotation, while gas is showing a broad distribution of rotation support, mostly in the ordered rotation regime. Angular momentum vectors of stars and dark matter do show then preferred alignment relative to each other, while gas is less well correlated with dark matter. The baryonic part of the halo does not counterrotate. The alignment is strongest in the near vicinity of the host or cluster halo.

Correlations between the main tidal field eigenvector and main inertia axis as well as angular momentum vector are shown, they resemble the one for the distribution between dark matter and baryonic angular momentum axis. The computations of the angular momentum of gas and star components do suffer uncertainties due to low particle numbers; higher resolution is needed to fix these. AGN

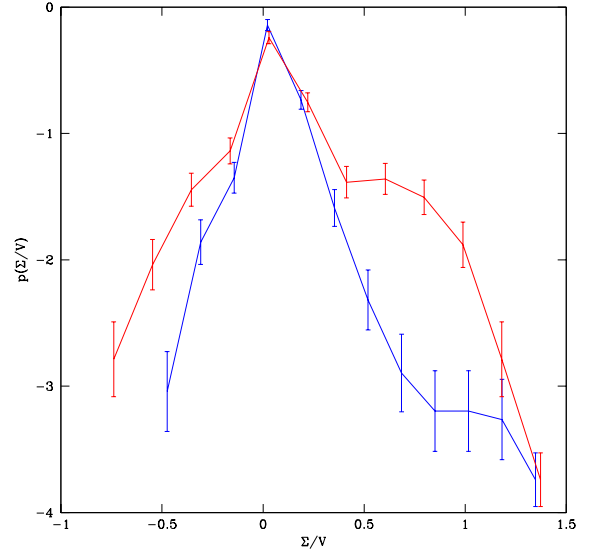


**Figure 12.**  $\Sigma/V$  distribution as given from AHF (in blue) and our own procedure (in red).

feedback should be included as well in later work to constrain over-cooling. It would be interesting for further investigations to divide the gas component into cold and hot gas or gas in the proximity of stars and gas farther away, allowing to condense the main contributions. The framework developed so far enables to follow the evolution of the properties from big structures at early times down to small structures at late times. In future work this redshift dependence shall be included in the analysis. The evolution of the most relevant scales for the smoothing of the tidal field would allow insight into which part of the angular momentum is generated at which epoch.

## ACKNOWLEDGEMENTS

We would like to thank Steffen Knollmann and Alexander Knebe for making the AHF code publicly available. PS is grateful for stimulating discussions with Romain Teyssier. All simulations presented are a subset of the TARKIN simulation set performed at the University of Padova. This work makes use of the NASA Astrophysics Data System.

## 6 APPENDIX: NUMERICAL ROBUSTNESS

Both AMIGA and our code were used to calculate the key features. Compared to each other, they show a very close agreement for the vast majority of the halos. We do see however, that our virial mass is off by a mean 8.5% of the total mass attributed to a halo. This is explained partly by the shift between the centers of the halos – center of mass or most bound particle – and the fact that we use another measure of the virial radius  $R_{vir}$ , which is used for calculations of  $M_{vir}$  and therefore angular momentum, spin parameter, shape parameters and  $\Sigma/V$  as well. Another possibility for mismatches comes from the fact that we restrict ourselves to halos with a minimum number of particles which is more restrictive than the 30 particles from AHF. An example comparison of the value for



$\Sigma/V$  calculated from all particles is given by figure 12: The bias towards galaxies with a minimum gas fraction and the fact that gas shows higher rotation support induces a higher fraction of highly rotationally supported systems in the left, while restriction to halos with more dark matter enhances the abundance of low rotationally supported systems with respect to the unbiased distribution from AHF values.

## REFERENCES

- Aragón-Calvo M. A., van de Weygaert R., Jones B. J. T., van der Hulst J. M., 2007, *ApJ*, 655, L5
- Barnes J., Efstathiou G., 1987, *ApJ*, 319, 575
- Basilakos S., Plionis M., Yepes G., Gottlöber S., Turchaninov V., 2006, *MNRAS*, 365, 539
- Bond J. R., Myers S. T., 1996, *ApJS*, 103, 1
- Borgani S., Murante G., Springel V., Diaferio A., Dolag K., Moscardini L., Tormen G., Tornatore L., Tozzi P., 2004, *MNRAS*, 348, 1078
- Brunino R., Trujillo I., Pearce F. R., Thomas P. A., 2007, *MNRAS*, 375, 184
- Bryan G. L., Norman M. L., 1998, *ApJ*, 495, 80
- Bullock J. S., Dekel A., Kolatt T. S., Kravtsov A. V., Klypin A. A., Porciani C., Primack J. R., 2001, *ApJ*, 555, 240
- Catelan P., Kamionkowski M., Blandford R. D., 2001, *MNRAS*, 320, L7
- Croft R. A. C., Di Matteo T., Springel V., Hernquist L., 2008, *ArXiv e-prints*
- Cuesta A. J., Betancort-Rijo J. E., Gottlöber S., Patiri S. G., Yepes G., Prada F., 2008, *MNRAS*, 385, 867
- De Lucia G., Kauffmann G., Springel V., White S. D. M., Lanzoni B., Stoehr F., Tormen G., Yoshida N., 2004, *MNRAS*, 348, 333
- Faltenbacher A., Jing Y. P., Li C., Mao S., Mo H. J., Pasquali A., van den Bosch F. C., 2008, *ApJ*, 675, 146
- Faltenbacher A., Li C., Mao S., van den Bosch F. C., Yang X., Jing Y. P., Pasquali A., Mo H. J., 2007, *ApJ*, 662, L71
- Gill S. P. D., Knebe A., Gibson B. K., 2004, *MNRAS*, 351, 399
- Hahn O., Carollo C. M., Porciani C., Dekel A., 2007, *MNRAS*, 381, 41
- Hahn O., Porciani C., Carollo C. M., Dekel A., 2007, *MNRAS*, 375, 489
- Hahn O., Teyssier R., Carollo C. M., 2010, *ArXiv e-prints*
- Hirata C. M., Mandelbaum R., Seljak U., Guzik J., Padmanabhan N., Blake C., Brinkmann J., Budavari T., Connolly A., Csabai I., Scranton R., Szalay A. S., 2004, *MNRAS*, 353, 529
- Knollmann S. R., Knebe A., 2009, *ApJS*, 182, 608
- Lau E. T., Nagai D., Kravtsov A. V., Zentner A. R., 2010, *ArXiv e-prints*
- Peebles P. J. E., 1969, *ApJ*, 155, 393
- Pereira M. J., Bryan G. L., Gill S. P. D., 2008, *ApJ*, 672, 825
- Porciani C., Dekel A., Hoffman Y., 2002a, *MNRAS*, 332, 325
- Porciani C., Dekel A., Hoffman Y., 2002b, *MNRAS*, 332, 339
- Sales L. V., Navarro J. F., Schaye J., Dalla Vecchia C., Springel V., Booth C. M., 2010, *ArXiv e-prints*
- Schaefer B. M., 2008, *ArXiv e-prints*
- Shandarin S. F., Zeldovich Y. B., 1989, *Reviews of Modern Physics*, 61, 185
- Sharma S., Steinmetz M., 2005, *ApJ*, 628, 21
- Springel V., 2005, *MNRAS*, 364, 1105
- Tegmark M., Blanton M. R., Strauss M. A., Hoyle F., Schlegel D., Scoccamarro R., Vogeley M. S., Weinberg D. H., Zehavi I., Berlind A., Budavari T., 2004, *ApJ*, 606, 702
- Valluri M., Debattista V. P., Quinn T., Moore B., 2010, *ArXiv e-prints*
- van den Bosch F. C., Abel T., Croft R. A. C., Hernquist L., White S. D. M., 2002, *ApJ*, 576, 21
- Wang Y., Park C., Yang X., Choi Y.-Y., Chen X., 2008, *ArXiv e-prints*
- Yang X., Mo H. J., van den Bosch F. C., Jing Y. P., Weinmann S. M., Meneghetti M., 2006, *MNRAS*, 373, 1159
- Zel'Dovich Y. B., 1970, *A&A*, 5, 84